Cloud phase classification using SLSTR measured brightness temperatures at 3.74, 10.85, 12.00 µm

Kameswara S. Vinjamuri, Marco Vountas, Vladimir Rozanov, Luca Lelli, Hartmut Boesch, John P. Burrows

PII: S0022-4073(26)00091-9
DOI: https://doi.org/10.1016/j.jqsrt.2026.109897
Reference: JQSRT 109897

To appear in: *Journal of Quantitative Spectroscopy and Radiative Transfer*

Received date : 19 August 2025
Revised date : 27 February 2026
Accepted date : 4 March 2026

Please cite this article as: K.S. Vinjamuri, M. Vountas, V. Rozanov et al., Cloud phase classification using SLSTR measured brightness temperatures at 3.74, 10.85, 12.00 µm. *Journal of Quantitative Spectroscopy and Radiative Transfer* (2026), doi: https://doi.org/10.1016/j.jqsrt.2026.109897.

Cloud phase classification using SLSTR measured brightness temperatures at 3.74, 10.85, 12.00 µm

Abstract

This study investigates the sensitivity of satellite-based brightness temperature measurements at 3.74, 10.85, and 12.00 µm with respect to the identification of water, ice, and mixed-phase clouds (MPC). Radiative transfer simulations computed by SCIATRAN reveal that the directional brightness temperature difference at 3.74 µm ($\Delta \mathrm{BT}_{3.74}$), which is dependent on scattering, enables water clouds and MPC separation from ice clouds. For water clouds and MPC, $\Delta \mathrm{BT}_{3.74}$ typically exceeds 2 K, whereas for ice clouds it remains below 2 K. To separate MPC from water clouds, we introduce the Liquid Cloud Probability Index (LCPI) based on cloud top temperature and absorption differences between water and ice at 10.85 and 12.00 µm. LCPI values generally exceed 0.4 for water clouds but fall below 0.4 for many MPC cases. The $\Delta \mathrm{BT}_{3.74}$ and LCPI approach is validated using the Sea and Land Surface Temperature Radiometer (SLSTR) dual-view data collocated with the 2B-CLDCLASS-LIDAR cloud phase product, showing over 90% accuracy in water and ice phase classification, and approximately 60% for MPC. This dual-view, multi-channel method enhances the detection of cloud phases, offering improved results for brightness temperature measurements.

Keywords:
SCIATRAN, Brightness temperature, Cloud phase, Dual-view

1. Introduction

Cloud phase identification retrieved from satellite-measured brightness temperature (BT), remains a challenging task [1–3]. These challenges arise because clouds can occur at varying cloud-top heights (CTH), optical thicknesses, and particle sizes, which significantly affect the Top-of-Atmosphere (TOA) observed BT. Bi-spectral approaches using the 10.80, 12.00 µm window region are commonly applied for cloud phase identification in operational algorithms due to the emissivity differences between water and ice [4–6]. A recent study by Mayer et al. [3] has shown that brightness temperature difference (BTD), 10.80–12.00 µm, has limited effectiveness in distinguishing cloud phases, especially for mid-level clouds with similar cloud-top temperatures. The BTD for identifying cloud phases also depends on surface temperatures and is influenced by the occurrence of mixed-phase clouds (MPC) [7–9]. MPC comprising water and ice particles usually occurs at high latitudes with cloud top temperatures below 273 K. These clouds pose a significant challenge for the retrieval of cloud optical properties [2, 7, 10, 11]. The presence of even small amounts of supercooled water droplets in MPC significantly affects their infrared spectral signature [12]. Studies have explored the inclusion of the 3.7 µm channel, enhancing phase sensitivity through its combined thermal emission and solar reflectance [13, 14]. While the tri-channel method (e.g., using 3.7, 10.80, and 12.00 µm) has shown improved sensitivity [15], its utility for MPC identification remains limited. It has also been shown that the BTD method of cloud phase classification becomes even more challenging over snow surfaces [16, 17]. Most studies have used single-view BT measurements from passive spectroradiometers to investigate cloud retrievals. Dual-view instruments such as the Along-Track Scanning Radiometer (ATSR), Advanced Along-Track Scanning Radiometer (AATSR), and Sea and Land Surface Temperature Radiometer (SLSTR) provide additional insights for atmospheric studies [18, 19]. Although dual-view measurements have considerably advanced atmospheric research, there is still a need for a comprehensive approach that fully exploits both spectral and angular information in order to characterize the cloud phases. Some cloud studies have investigated the use of dual-view measurements at 3.7 µm [18, 20, 21], but these have been limited to cirrus clouds. A comprehensive investigation into cloud phase detection using dual-view BT at 3.74 µm and BTD at 10.85 and 12.00 µm has not yet been carried out.

In this study, a theoretical radiative transfer-based analysis is conducted using simulated daytime brightness temperatures at 3.74, 10.85, and 12.00 µm, considering variations in cloud microphysical properties and surface temperature (T_s). A key objective is to develop a physically-based method for discriminating between cloud phases using brightness temperatures. To this end, this study proposes a simple dual-view approach at 3.74 µm, complemented by a formulation involving BTD at 10.85 and 12.00 µm, to distinguish between water and ice clouds, as well as possible MPC cases. In the latter part of the study, the proposed phase separation technique is validated using real brightness temperature observations from the SLSTR instrument on the Sentinel-3A platform and comparisons with the 2B-CLDCLASS-LIDAR product [22, 23]. The SLSTR instrument has two near-simultaneous views, in near-nadir and oblique angles. The nadir view is directed directly downwards, while the oblique view angle is 55°. The 2B-CLDCLASS-LIDAR data set provides cloud phase classification based on CloudSat radar data and CALIPSO lidar measurements. In particular, for MPC detection, the radar is more sensitive to larger ice particles, while the lidar is more responsive to smaller liquid droplets, providing a reliable assessment of the cloud phase. To improve the chances of MPC detection, collocations between SLSTR and 2B-CLDCLASS-LIDAR are carried out at high northern latitudes ($> 60^\circ$ N). These regions are characterized by ocean and ice surfaces, which exhibit high emissivities in the considered thermal infrared bands. Finally, the study finishes with a conclusion about how the presented approach discriminates the cloud phase, with particular emphasis on the improved detection of MPC cases using dual-view satellite measurements.

2. Method

To simulate brightness temperatures at the TOA, the SCIATRAN radiative transfer is used for three cloud types (water, ice, and MPC) in a pseudo-spherical geometry. This setup accurately accounts for scattered solar light, thermal emission, and gaseous absorption simultaneously across different wavelengths and viewing geometries [24, 25]. The spectral configurations were based on the Sentinel-3A SLSTR thermal channels, specifically the S7, S8, and S9 bands, with measured central wavelengths (spectral bandwidths) of 3.74 µm (0.38 µm), 10.85 µm (0.9 µm), and 12.00 µm (1 µm). The simulated BT spectra are integrated over the SLSTR spectral response functions to ensure consistency with the observations. The simulations assume clouds to be vertically homogeneous in the atmosphere (effective representation at the TOA). Simulations are performed varying cloud optical depth (COD) values of 1, 2, 3, 5, 10, 15, 20, and 30. COD values greater than 30 are not presented, as the BTD values become saturated at higher COD values [2, 3]. A constant solar zenith angle of 55° is assumed. For water clouds, effective droplet radii (r_{eff}) of 4 and 16 µm are selected as the lower and upper extremes. For ice clouds, maximal particle dimensions ($D_{\max}$) of 45 and 180 µm are considered as the limits. The optical properties of water clouds are obtained from a database generated using the Lorenz–Mie theory

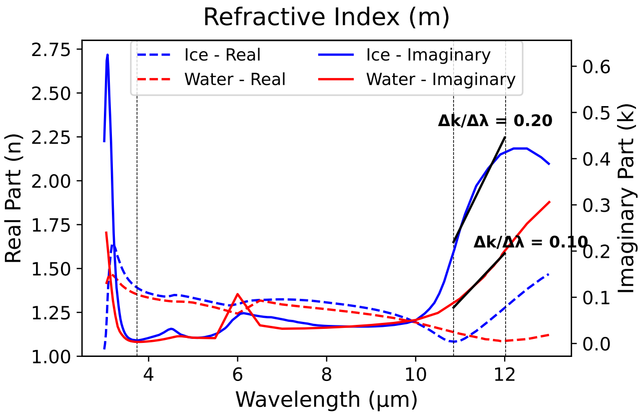

Figure 1: The plot shows the spectral variation of the real and imaginary parts of the complex refractive index for water and ice. The vertical lines indicate the channels used in this study. The slopes of the imaginary part of the complex refractive index for water and ice between 10.85 µm and 12.00 µm are provided in black.

[26], assuming a gamma size distribution [25]. Optical properties for non-spherical ice particles are derived from Yang's database, using a moderately rough solid column habit with a gamma particle size distribution [27]. Since the objective of this work is to separate the cloud phases rather than the ice habits, a solid column shape is considered for ice crystals in ice clouds and MPC. A previous study by Mayor et al [3] has shown that ice crystal habits have a minimal impact on BTD values. For MPC, varying proportions of liquid and ice are quantified using the ice fraction of the total optical depth ($\mathrm{IF_{cod}}$), which is the ratio of ice COD to total COD (a value of 0 indicates water clouds, a value of 1 indicates ice clouds, and intermediate values indicate MPC). In this study, the $\mathrm{IF_{cod}}$ values considered for MPC are 0.2, 0.4, 0.5, 0.6, and 0.8. The extinction coefficient, single scattering albedo, and asymmetry parameter of MPC are computed as weighted combinations of water and ice contributions, with detailed formulations provided in the Appendix A.

The atmospheric temperature and pressure are taken from the U.S. Standard Atmosphere profile for water and ice clouds. For MPC, the temperature and pressure profiles are used from the McLinden climatology database provided by SCIATRAN. To make it consistent with the validation (see more in section 4), profiles corresponding to the high latitudes for the month of May

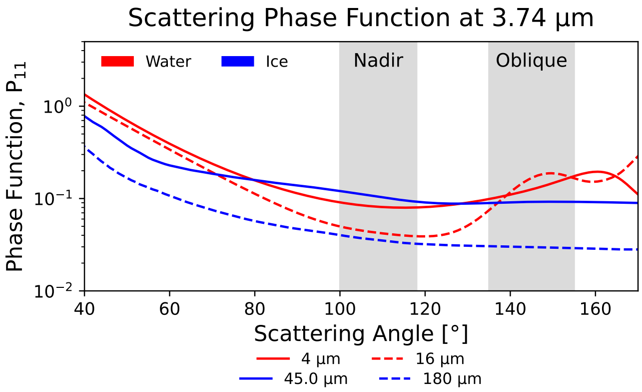

Figure 2: The plot shows the scattering phase functions at 3.74 µm for water droplets and ice crystals. The shaded regions indicate SLSTR-relevant viewing geometries for nadir and oblique views.

are used. CTH (and its corresponding cloud top temperature (CTT) from the profiles) is varied to represent typical values associated with different cloud phases, i.e., water, ice, and MPC. CTH (CTT) for water clouds are set to 1 km (281.7 K), 2 km (275.2 K), 4 km (262.2 K), and 6 km (249.2 K). For ice clouds, the CTH (CTT) values are set to 4 km (262.2 K), 6 km (249.2 K), 8 km (236.2 K), 10 km (223.3 K), and 12 km (216.7 K). For MPC, CTH (CTT) of 1 km (263.4 K), 2 km (259.3 K), 3 km (254.5 K), 4 km (249.5 K), 5 km (243.9 K), and 6 km (238.1 K) are considered. For all simulations, a cloud geometrical thickness of 500 m is assumed, and temperature within the cloud layer follows the vertical temperature gradient of the assigned atmospheric profile. A range of surface temperatures, 290 K, 273 K, and 260 K, is used for the simulations. Water vapor absorption is modeled consistently with the corresponding atmospheric temperature profiles. A surface emissivity of 1 is assumed, which is representative of the ocean and ice surfaces.

3. Results

Figure 1 presents the spectral variation of the complex refractive index for water and ice [28, 29] with vertical lines indicating the bands used in the study. At 3.74 µm, scattering dominates due to a relatively high real part and a low imaginary part of the refractive index. In contrast, absorption, associated with the imaginary part of the refractive index, increases

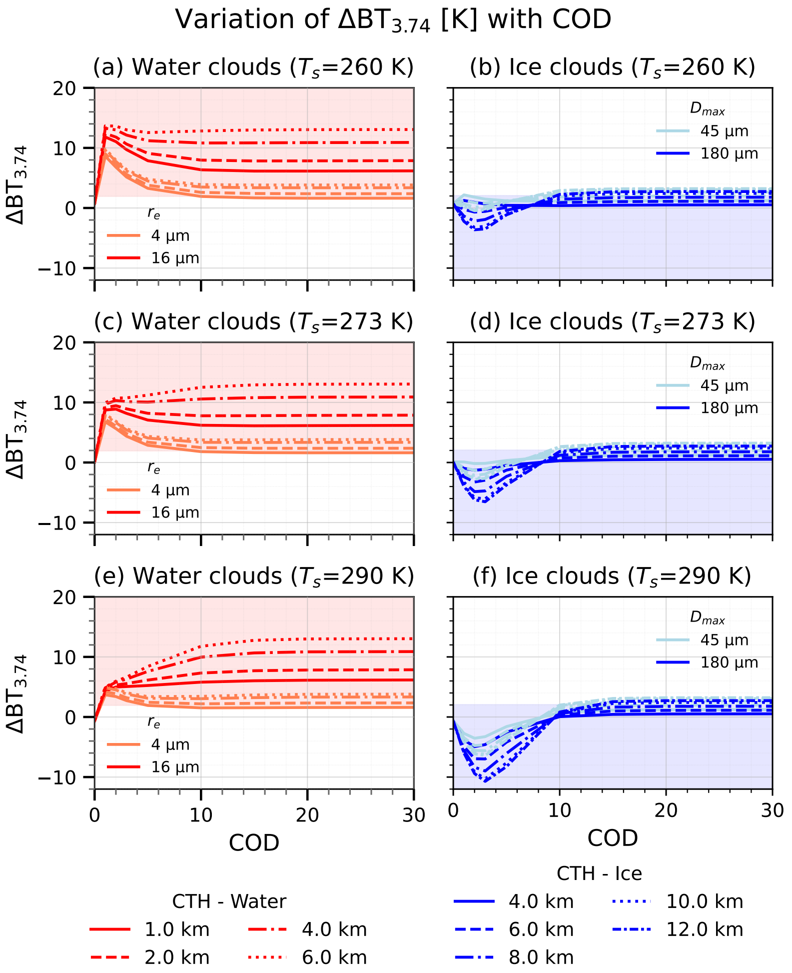

Figure 3: The plots show the variation of $\Delta BT_{3.74}$ at 3.74 µm with COD for water and ice clouds above three different surface temperatures (T_s = 260 K, 273 K, 290 K). Subplots (a), (c), and (e) correspond to water clouds with r_{eff} of 4 µm and 16 µm; panels (b), (d), and (f) represent ice clouds with $D_{\max}$ of 45 µm and 180 µm. The shaded regions represent the 2 K threshold for separating water and ice clouds.

significantly beyond 10 µm for both water and ice, indicating absorption-dominated regimes. Using this knowledge, the scattering-dominant wavelength of 3.74 µm is used to analyze the angular distribution of scattered radiation through the phase functions, as shown in Fig.2, for different particle sizes. Water exhibits noticeably higher phase function values at scattering angles greater than approximately 130°, whereas ice displays more constant values between 100° and 170°. Assuming that the oblique view of SLSTR corresponds to scattering angles between 130° and 160°, and the nadir view to angles between 100° and 120° (shown as shaded regions in the plot), the BT difference between the two views is expected to vary depending on the cloud phase. Given the increase of phase function values for water in the 130°–160° range compared to 100°–120°, the BT difference between these regions is expected to be larger for water clouds than for ice clouds. This difference is quantified as:

$$\Delta \mathrm{BT}_{3.74} = \mathrm{BT}_{3.74}^{\mathrm{oblique}} - \mathrm{BT}_{3.74}^{\mathrm{nadir}} \tag{1}$$

To compute the $\Delta\mathrm{BT}_{3.74}$ using SCIATRAN simulations, this study investigated specific geometries corresponding to nadir and oblique viewing angles. The oblique and nadir scattering angles correspond to angles approximately 147.47° (SZA=55°, VZA=55°, RAA=140°) and 118.26° (SZA=55°, VZA=10°, RAA=50°), respectively. Using the available viewing geometries, the resulting $\Delta\mathrm{BT}_{3.74}$ for both water and ice clouds for different T_s are shown in Fig.3. $\Delta\mathrm{BT}_{3.74}$ values of water clouds consistently exceed 2 K across all T_s, showing the strong angular contrast between the observations at different viewing angles at 3.74 µm. Larger droplets (16 µm) produce higher $\Delta\mathrm{BT}_{3.74}$ compared to smaller ones (4 µm), with the separation between them being most evident at higher COD. For water clouds having larger r_{eff}, the $\Delta\mathrm{BT}_{3.74}$ are larger than 5 K for all T_s. Even though the values of $\Delta\mathrm{BT}_{3.74}$ for water clouds with smaller r_{eff} are less than for the larger r_{eff}, the values of $\Delta\mathrm{BT}_{3.74}$ are still greater than 2 K. This difference between smaller and larger droplets in the water clouds is due to the larger gradient for larger water droplets in the phase functions between the two views (Fig.2). The water clouds with CTH at 1 km, consisting of smaller r_{eff}, show $\Delta\mathrm{BT}_{3.74}$ values of approximately 2 K. In contrast, for ice clouds, phase function differences between the views are minimal at 3.74 µm. Across all T_s and particle sizes, $\Delta\mathrm{BT}_{3.74}$ remains below 2 K and is often negative for COD values less than 10. Over warm surfaces (T_s = 290 K), $\Delta\mathrm{BT}_{3.74}$ values for ice clouds are relatively large negative magnitudes compared to cold surfaces (T_s = 260 K). Ice clouds composed of larger D_{max} (180 µm) exhibit lower values as compared to ice clouds with smaller D_{max} (45 µm) across all T_s. For COD greater than 10, $\Delta\mathrm{BT}_{3.74}$ values range from 0 to 2 K. However, ice clouds are usually optically thin, and such optically thick ice clouds are rare. In both cases of water and ice clouds, T_s

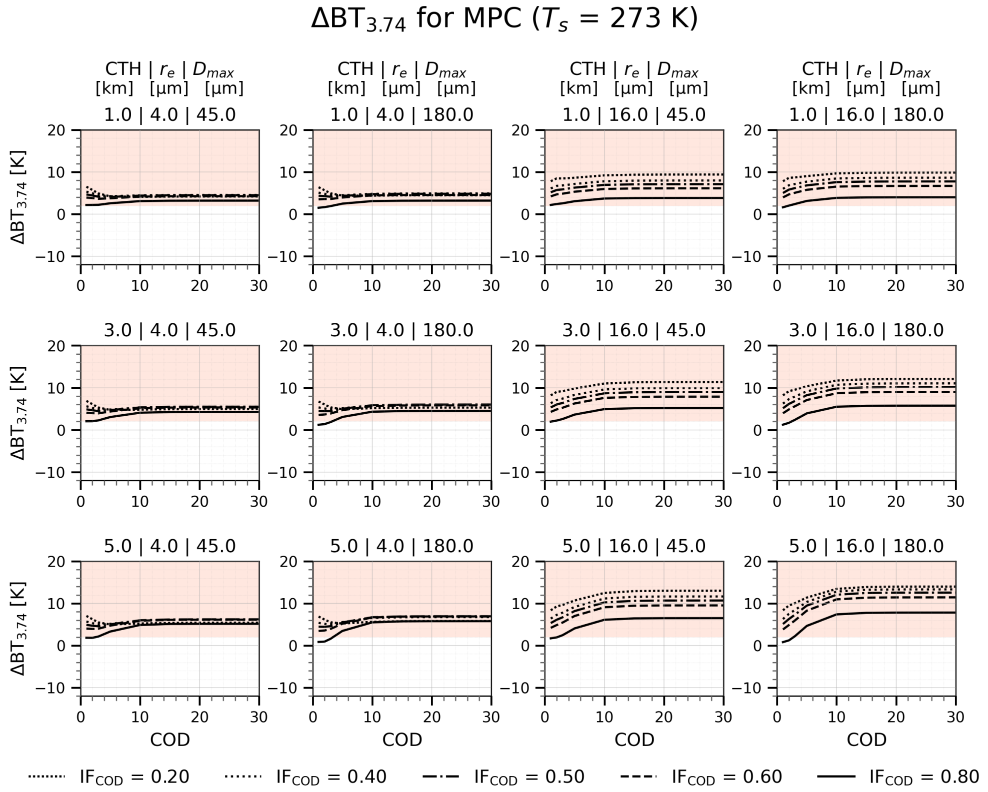

Figure 4: The plot shows the variation of $\Delta\mathrm{BT}_{3.74}$ at 3.74 μm with COD for MPC as a function of $\mathrm{IF}_{\mathrm{cod}}$, at T_s of 273 K. Each row corresponds to a different CTH (1 km, 3 km, 5 km from top to bottom). Each column represents a different combination of r_{eff} and D_{max}. The shaded region represents the 2 K threshold.

impacts more strongly the $\Delta\mathrm{BT}_{3.74}$ for COD values less than 10.

For MPC, Fig.4 presents the $\Delta\mathrm{BT}_{3.74}$ at $T_s = 273$ K at CTH 1 km, 3 km, 5 km (results for CTH 2 km, 4 km, 6 km and results for $T_s = 260$ K and $T_s = 290$ K are given in the appendix section: Fig.B.8, Fig.B.9 and Fig.B.10). Each panel in the figure represents a different combination of CTH, r_{eff}, D_{max} for MPC. Each row represents the increasing CTH levels. The first two columns show the combination of smaller water droplets ($r_{\mathrm{eff}} = 4$ μm) with two extreme crystal sizes ($D_{\mathrm{max}} = 45$, 180 μm) in the MPC, while the following two columns show the combination of larger water droplets ($r_{\mathrm{eff}} = 16$ μm) with two extreme crystal sizes ($D_{\mathrm{max}} = 45$, 180 μm) in the

MPC. At $T_s = 273$ K, for most of the cases, the $\Delta\mathrm{BT}_{3.74}$ values for MPC are greater than 2 K. MPC composed of smaller water droplets have lower $\Delta\mathrm{BT}_{3.74}$ values and is less sensitive to $\mathrm{IF}_{\mathrm{cod}}$ as compared to MPC with larger water droplets (for all CTH) (see comparisons between columns 1,2 to 3,4 in Fig. 4). At low COD values, as the CTH increases, the $\Delta\mathrm{BT}_{3.74}$ values for MPC are less than 2 K. Similar to water clouds, the T_s has a lesser impact as COD values become higher (COD ≥ 10). For COD values less than 10, as T_s increases, the $\Delta\mathrm{BT}_{3.74}$ values become closer to 0 K (especially when $\mathrm{IF}_{\mathrm{cod}} = 0.8$), making it difficult to distinguish them from ice clouds. MPC with high $\mathrm{IF}_{\mathrm{cod}}$ (when $\mathrm{IF}_{\mathrm{cod}} = 0.8$), at COD values less than 5, over warmer T_s (290 K), the $\Delta\mathrm{BT}_{3.74}$ are always less than 2 K (Fig. B.10). Overall, in most cases, the presence of water results in the MPC $\Delta\mathrm{BT}_{3.74}$ values becoming greater than 2 K, except for MPC with low COD values over warmer surfaces.

While the $\Delta\mathrm{BT}_{3.74}$ helps distinguish ice clouds from water-containing ones, it becomes less effective for differentiating water clouds from MPC (as both water and MPC have values greater than 2 K). To address this issue, this study uses the spectral characteristics of cloud absorption in the thermal infrared bands. As discussed above, the absorption increases from 10.85 to 12.00 µm for both water and ice. However, between 10.85 and 12.00 µm, the rate of increase (i.e., the slope) is notably steeper for ice than for water (Fig. 1). This results in stronger absorption at 12.00 µm for ice clouds relative to 10.85 µm, producing larger BTD. Water clouds, on the other hand, exhibit a more gradual slope and hence smaller BTD values. From the previous studies, water clouds often exhibit BTD values of less than 1 K [30, 31]. Additionally, water clouds are typically warmer, with cloud-top temperatures exceeding 260 K. These two properties, i.e., low BTD and relatively warm temperatures, serve as reliable indicators of distinguishing water clouds from the rest. To incorporate these traits quantitatively, we formulated the Liquid Cloud Probability Index (LCPI) as:

$$\mathrm{LCPI} = \frac{1}{1 + e^{-(\mathrm{BT}_{12.00} - 260)}} \cdot \frac{1}{1 + e^{(\mathrm{BT}_{10.85} - \mathrm{BT}_{12.00}) - 1}} \tag{2}$$

The first term, involving $\mathrm{BT}_{12.00}$, increases when the temperature exceeds 260 K, typical of water clouds, and decreases for colder cloud tops, as found in ice or MPC. The second term increases when the BTD is less than 1 K, a characteristic of water clouds. By multiplying these two terms, the LCPI attains high values only when both conditions are satisfied (warm cloud top temperatures and low BTD), strongly indicating the presence of water clouds.

If either the temperature is low or the BTD is large, the LCPI becomes low, effectively indicating ice or MPC conditions. To visualize this behavior, LCPI versus $\Delta\mathrm{BT}_{3.74}$ is plotted in Fig. 5 and Fig. 6. In these figures, the LCPI is on the horizontal axis and $\Delta\mathrm{BT}_{3.74}$ is on the vertical axis. Each row in these figures displays the distribution of simulated cloud cases, colored by a third physical parameter (COD, $\mathrm{IF}_{\mathrm{cod}}$ in Fig. 5 and CTH, T_s in Fig. 6). This illustrates how these physical parameters influence the spread of cloud types using LCPI and $\Delta\mathrm{BT}_{3.74}$.

Water clouds generally exhibit high LCPI values (typically > 0.4), particularly under optically thick conditions, as illustrated in Fig. 5a. Exceptions occur for water clouds at CTH values close to 6 km, where LCPI values can be lower (Fig. 6a). MPC occurs across a wide range of LCPI values, with low LCPI values observed for COD values greater than 5, as shown in Fig. 5b. There are cases where the LCPI values of optically thick MPC are also high, making it difficult to distinguish from water clouds. These optically thick MPC occur at CTH values less than 2 km, i.e., MPC with relatively warmer CTT (Fig. 5b, Fig. 6b). This implies that distinguishing MPC from water clouds becomes particularly challenging at lower CTH. MPC with high $\mathrm{IF}_{\mathrm{cod}}$ (> 0.6) also have high LCPI values, when their COD is less than 5 and with high T_s (Fig. 5b, Fig. 5d, Fig. 6d). As a result, these MPC may have similar brightness signatures to those of pure phase clouds. Even though there are cases where MPC and water clouds have similar LCPI values, most overlapping cases using $\Delta\mathrm{BT}_{3.74}$ are identified using LCPI. For ice clouds, the LCPI values are typically low, often close to zero. However, some ice clouds show LCPI values exceeding 0.4, particularly when they occur over high T_s and low CTH (4 km) (Fig. 6a, Fig. 6c). Optically thin ice clouds over warm T_s also exhibit high LCPI values due to significant thermal emission from the underlying surface (Fig. 5a, (Fig. 6c). However, these cases can be effectively distinguished using low $\Delta\mathrm{BT}_{3.74}$ values. T_s plays a critical role in the distinguishing of MPC from ice clouds using $\Delta\mathrm{BT}_{3.74}$, as optically thin MPC over warm surfaces may exhibit very low $\Delta\mathrm{BT}_{3.74}$ similar to those of ice clouds (Fig. 5b, Fig. 6d). Overall, $\Delta\mathrm{BT}_{3.74}$ serves as a reliable indicator for distinguishing between water and ice clouds with a 2 K threshold, while the LCPI threshold of 0.4 separates possible MPC cases from water clouds.

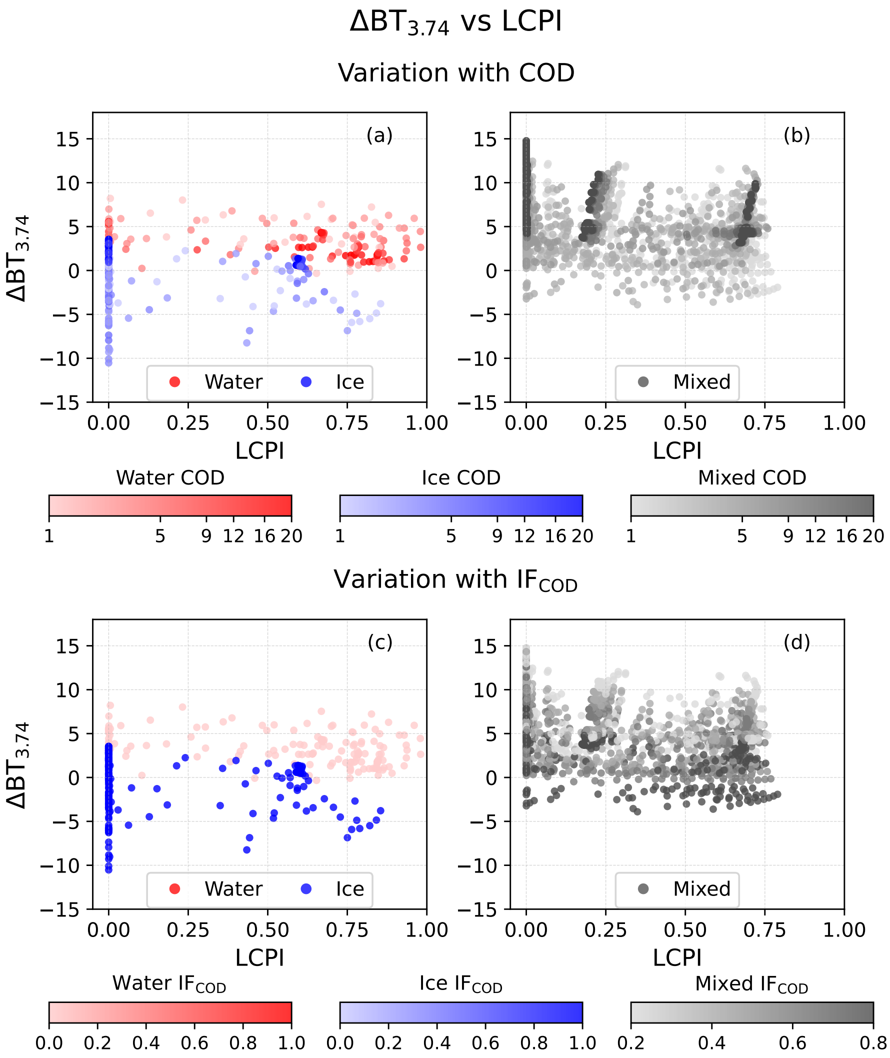

Figure 5: The plots show the variation of $\Delta BT_{3.74}$ with the LCPI for simulated water, ice, and MPC. Subplots (a) and (c) display water and ice clouds, while (b) and (d) show MPC. The top row is color-coded by COD, and the bottom row by IF_{cod}.

4. SLSTR validation with 2B-CLDCLASS-LIDAR

Using the SCIATRAN-based results from the previous section, the two phase-sensitive parameters, $\Delta BT_{3.74}$ and LCPI, are derived from SLSTR measurements and validated by comparison with 2B-CLDCLASS-LIDAR

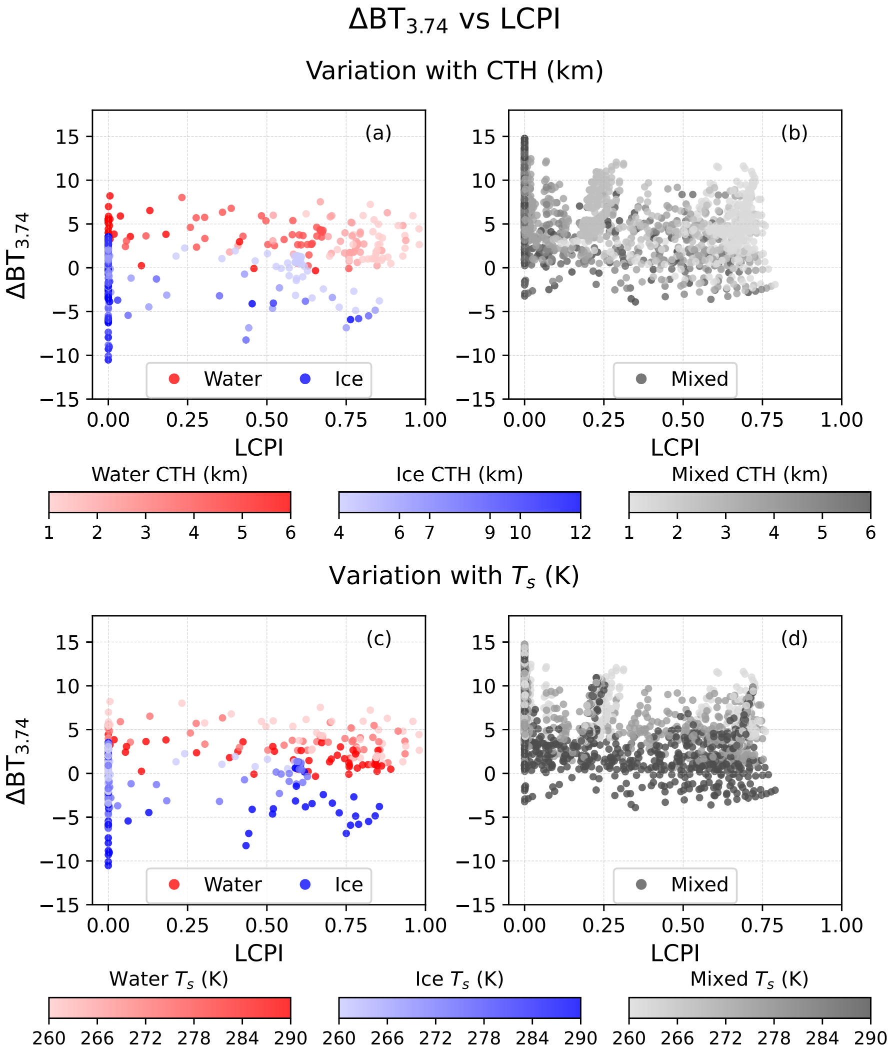

Figure 6: Same as Fig. 5 but top row is color-coded by CTH, and the bottom row by T_s.

data. The BT data at 3.74 µm (for both views), 10.85 µm, and 12.00 µm are available at 1 km spatial resolution from the SLSTR-L1B data product. The oblique views of SLSTR are parallax-adjusted to the nadir view, as mentioned in Virtanen et al. [19]. Both the SLSTR and 2B-CLDCLASS-LIDAR data are collocated with a distance of 2 km and a temporal window of ±5 minutes at high latitudes (above 60° N) on the 3rd of May, 2020.

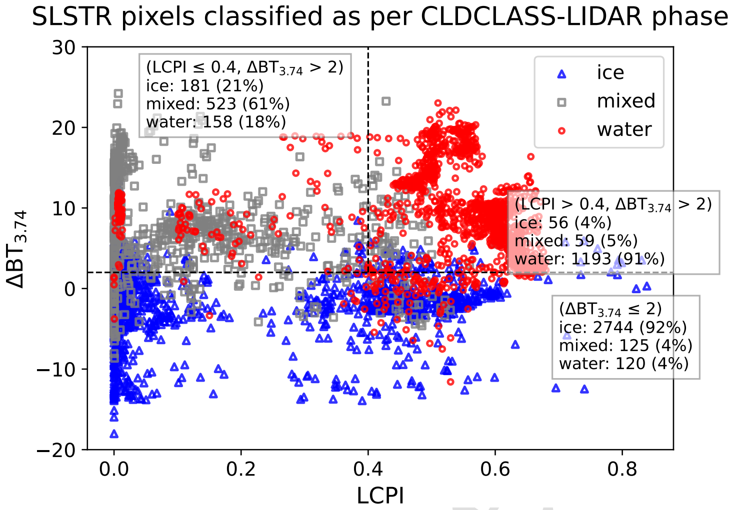

Figure 7: The plot shows the distribution of SLSTR cloud pixels in the $\Delta BT_{3.74}$ vs LCPI space, color-coded by cloud phase from the 2B-CLDCLASS-LIDAR product for the day 3rd May 2020. The plot is divided into three regions: (1) $\Delta BT_{3.74} \leq 2$ K, where ice clouds dominate; (2) $\Delta BT_{3.74} > 2$ K and LCPI > 0.4, where water clouds dominate; and (3) $\Delta BT_{3.74} > 2$ K and LCPI ≤ 0.4, representing MPC conditions. The percentages represent the relative frequency of each cloud phase within that region.

The analysis is restricted to cases with vertically homogeneous cloud phases from 2B-CLDCLASS-LIDAR data. Fig.7 represents the LCPI vs $\Delta BT_{3.74}$ plot calculated from SLSTR and color coded by the phase information from the 2B-CLDCLASS-LIDAR product. The plot is divided into three regions, based on the results presented in Section 3, with each region corresponding to a dominant cloud phase. These divisions are constructed to encompass the majority of ice, water, and MPC cases as characterized by their LCPI and $\Delta BT_{3.74}$ values. The three divisions are defined as: (1) Ice-dominated regime ($\Delta BT_{3.74} \leq 2$ K), (2) Water-dominated regime ($\Delta BT_{3.74} > 2$ K and LCPI > 0.4), and (3) MPC regime ($\Delta BT_{3.74} > 2$ K and LCPI ≤ 0.4). In the $\Delta BT_{3.74} \leq 2$ K region, 92% of pixels are classified as ice phase, with only 4% each for water and MPC, demonstrating that low directional contrast is a strong indicator in separating ice clouds from water-consisting clouds. Conversely, in the region with LCPI > 0.4 K and $\Delta BT_{3.74} > 2$ K (upper right), 91% of pixels are water clouds, indicating the presence of liquid-only clouds. In the region where the liquid droplet signature is evident ($\Delta BT_{3.74} > 2$ K) but LCPI values remain low, likely due to strong absorption by ice and lower CTT, MPC are detected in nearly 60% of the cases. As the plots show using only LCPI alone, i.e., BTD between 10.85 µm and 12.00 µm, it is very hard to distinguish between water and ice clouds (as also described in the previous works mentioned in Section 1). The addition of oblique and nadir views from 3.74 µm enhanced the detection capability, and a combination with 10.85 µm and 12.00 µm makes it possible to distinguish MPC under many conditions, with exceptions described in Section 3. These results demonstrate the complementary nature of solar and thermal emission at 3.74 µm, as well as thermal emission at 10.85 µm and 12.00 µm, in detecting complex cloud phases in passive dual-view satellite measurements.

5. Conclusions

This study demonstrates the value of combining dual-view brightness temperature measurements at 3.74 µm ($\Delta BT_{3.74}$), with brightness temperature differences at 10.85 µm and 12.00 µm to enable cloud phase discrimination using satellite remote sensing. Using detailed radiative transfer simulations with SCIATRAN, we establish that the directional brightness temperature difference at 3.74 µm provides a physical basis for separating ice from water-containing clouds. However, this alone proves insufficient for isolating mixed-phase clouds (MPC) from water clouds. To enhance sensitivity, we introduce the Liquid Cloud Probability Index (LCPI), a temperature and brightness temperature difference-based indicator derived using 10.85 µm and 12.00 µm measurements. The LCPI values are high for water clouds, and low for ice-consisting clouds in most cases. From the simulated results, distinguishing MPC and water clouds becomes more challenging when MPC occurs at CTH less than 2 km, and distinguishing MPC and ice clouds becomes more challenging for optically thin cases and warm surfaces. Surface temperatures play a crucial role, especially for optically thin MPC. Validation of LCPI-$\Delta BT_{3.74}$ values from SLSTR data with the 2B-CLDCLASS-LIDAR product demonstrated 90% classification accuracy in distinguishing between water and ice clouds and 60% for MPC. This makes it a useful approach, especially when the traditional brightness temperature differences method at 10.85 µm and 12.00 µm has its limitations. It also manages the identification of MPC regimes that are often misclassified in most of the existing methods. Overall, this study demonstrates the potential of using the brightness temperatures at 3.74, 10.85, and 12.00 µm in passive remote sensing for cloud phase retrieval. The methodology applies to current dual-view sensors, such as SLSTR. It provides a foundation for future multi-angle missions seeking to improve the cloud retrievals, their radiative impacts, and their changes in a warming world.

Appendix A. Optical Properties of MPC

For MPC composed of both liquid and ice particles, the total COD is expressed as

$$\tau = \tau_{\text{ice}} + \tau_{\text{water}}, \tag{A.1}$$

The bulk single-scattering properties i.e., the extinction efficiency $\langle Q_e \rangle$, single-scattering albedo $\langle \omega_0 \rangle$, and asymmetry parameter $\langle g \rangle$ are defined as

$$\langle Q_e \rangle = \text{IF}_{\text{COD}} \cdot \langle Q_{e,\text{ice}} \rangle + (1 - \text{IF}_{\text{COD}}) \cdot \langle Q_{e,\text{water}} \rangle \tag{A.2}$$

$$\langle \omega_0 \rangle = \frac{\text{IF}_{\text{COD}} \cdot \langle Q_{s,\text{ice}} \rangle + (1 - \text{IF}_{\text{COD}}) \cdot \langle Q_{s,\text{water}} \rangle}{\langle Q_e \rangle}, \tag{A.3}$$

$$\langle g \rangle = \frac{\text{IF}_{\text{COD}} \cdot \langle Q_{s,\text{ice}} \rangle \cdot g_{\text{ice}} + (1 - \text{IF}_{\text{COD}}) \cdot \langle Q_{s,\text{water}} \rangle \cdot g_{\text{water}}}{\langle Q_s \rangle}. \tag{A.4}$$

where

$$\langle Q_s \rangle = \text{IF}_{\text{COD}} \cdot \langle Q_{s,\text{ice}} \rangle + (1 - \text{IF}_{\text{COD}}) \cdot \langle Q_{s,\text{water}} \rangle \tag{A.5}$$

$\text{IF}_{\text{COD}} \in [0, 1]$ denotes the contribution of ice to the total extinction.

Appendix B. $\Delta\text{BT}_{3.74}$ plots of MPC at various T_s.

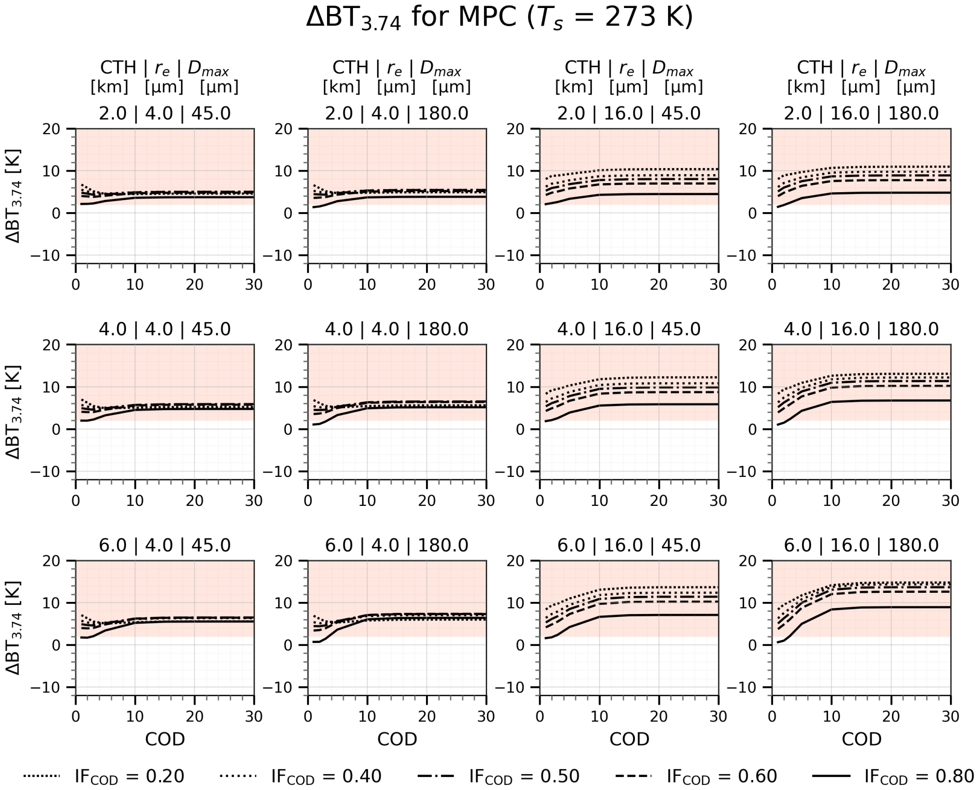

Figure B.8: Same as Fig. 4 but at CTH 2 km, 4 km, 6 km.

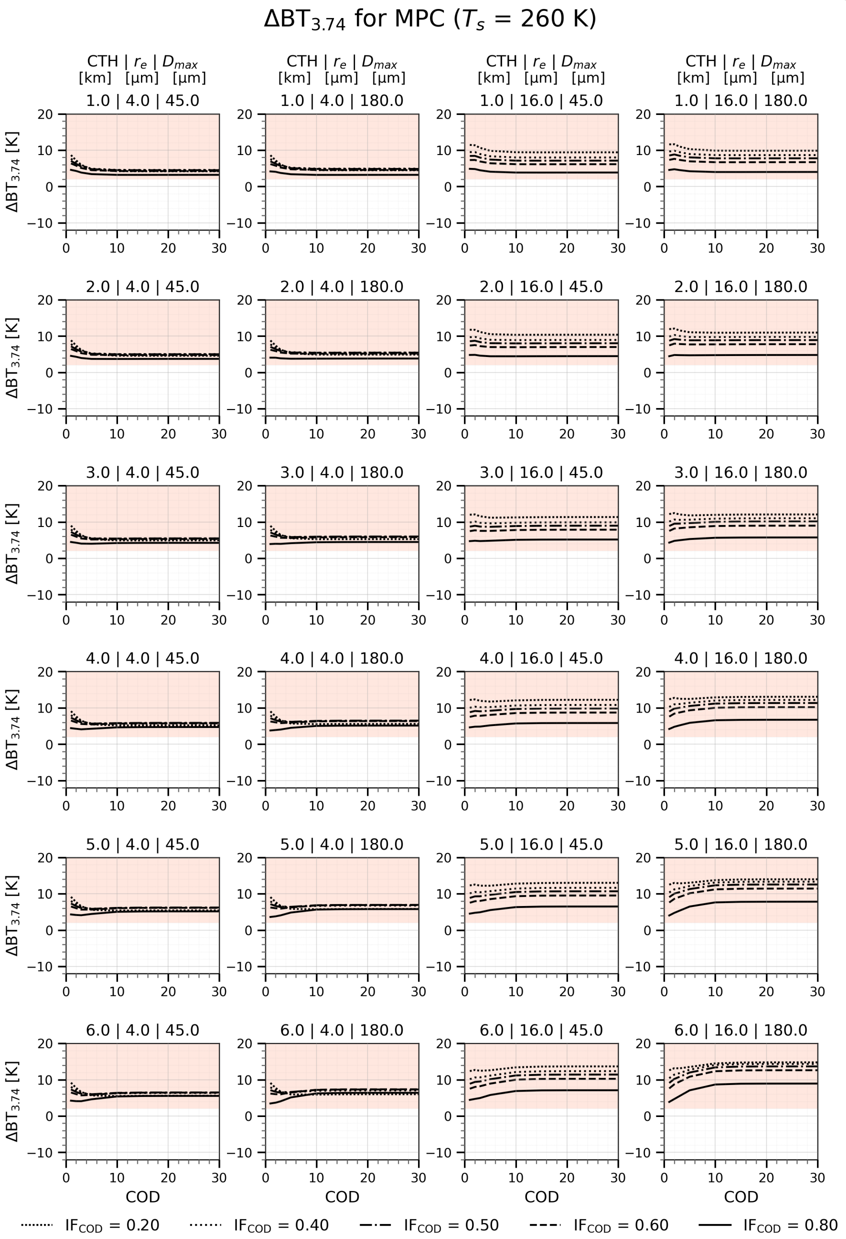

Figure B.9: Same as Fig. 4 but for T_s of 260 K at all considered CTH.

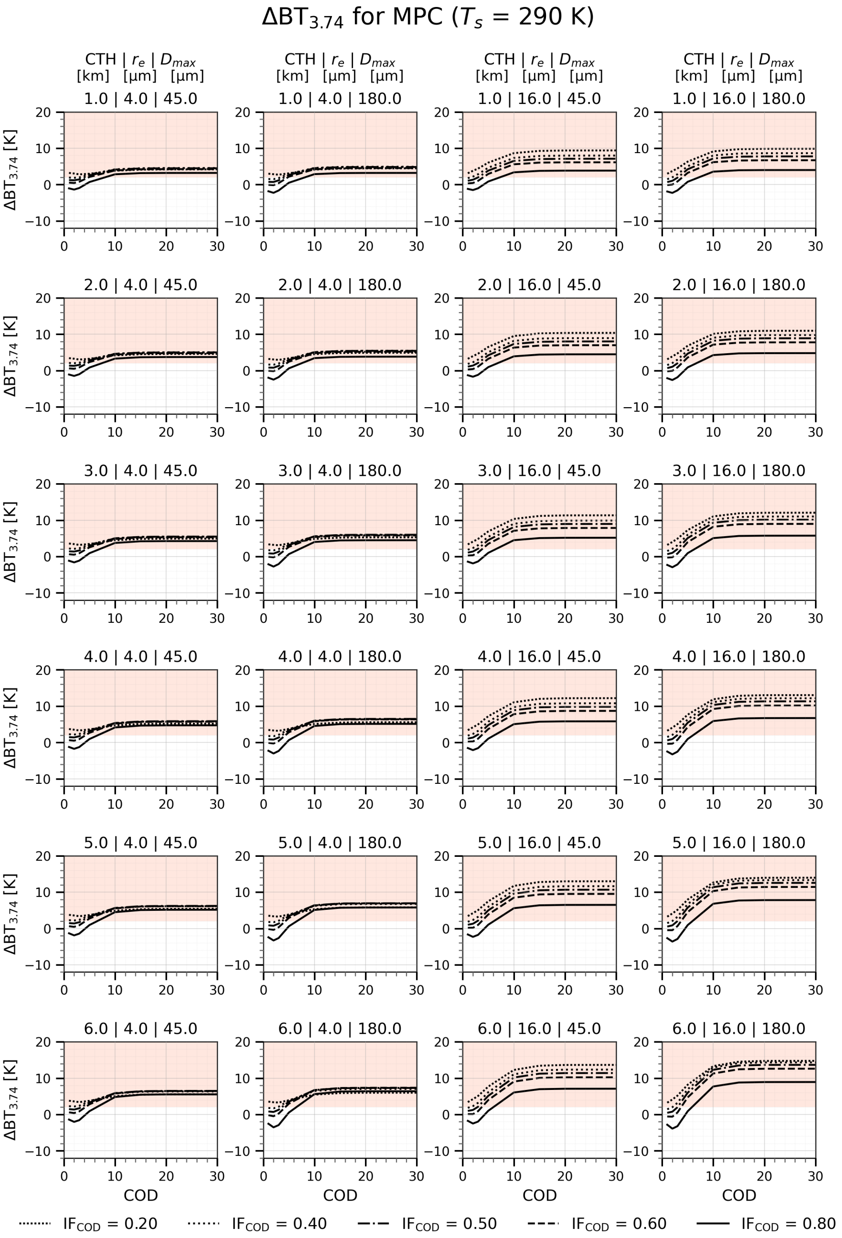

Figure B.10: Same as Fig. 4 but for T_s of 290 K at all considered CTH.

Data availability

SCIATRAN is available from the Institute of Environmental Physics (IUP) (https://www.iup.uni-bremen.de/sciatran/). Contains modified Copernicus Sentinel data [2020]. The SLSTR L1B data can be accessed from the Copernicus Data Space Ecosystem (CDSE) https://browser.dataspace.copernicus.eu/. The 2B-CLDCLASS-LIDAR data can be accessed at https://www.cloudsat.cira.colostate.edu/data-products/2b-cldclass-lidar; last access: February 2024.

Declaration of competing interest

The authors declare they have no competing interests.

References

[1] Strabala K. I, Ackerman S. A, Menzel W. P, Cloud Properties inferred from 8-12 µm Data, Journal of Applied Meteorology 33 (2) (02 1994). `http://dx.doi.org/10.1175/1520-0450(1994)033<0212:CPIFD>2.0.CO;2`.

[2] Nasiri S. L, Kahn B. H, Limitations of Bispectral Infrared Cloud Phase Determination and Potential for Improvement, Journal of Applied Meteorology and Climatology 47 (11) (2008) 2895 – 2910. `http://dx.doi.org/10.1175/2008JAMC1879.1`.

[3] Mayer J, Mayer B, Bugliaro L, Meerkötter R, Voigt C, How well can brightness temperature differences of spaceborne imagers help to detect cloud phase? A sensitivity analysis regarding cloud phase and related cloud properties, Atmospheric Measurement Techniques 17 (17) (2024) 5161–5185. `http://dx.doi.org/10.5194/amt-17-5161-2024`.

[4] Chylek P, Robinson S, Dubey M. K, King M. D, Fu Q, Clodius W. B, Comparison of near-infrared and thermal infrared cloud phase detections, Journal of Geophysical Research: Atmospheres 111 (D20) (2006). `http://dx.doi.org/10.1029/2006JD007140`.

[5] Rosenfeld D, Liu G, Yu X, Zhu Y, Dai J, Xu X, Yue Z, High-resolution (375 m) cloud microstructure as seen from the NPP/VIIRS satellite imager, Atmospheric Chemistry and Physics 14 (5) (2014) 2479–2496. `http://dx.doi.org/10.5194/acp-14-2479-2014`.

[6] Stengel M, Stapelberg S, Sus O, Finkensieper S, Würzler B, Philipp D, Hollmann R, Poulsen C, Christensen M, McGarragh G, Cloud_cci Advanced Very High Resolution Radiometer post meridiem (AVHRR-PM) dataset version 3: 35-year climatology of global cloud and radiation properties, Earth System Science Data 12 (1) (2020) 41–60. `http://dx.doi.org/10.5194/essd-12-41-2020`.

[7] Spangenberg D. A, Minnis P, Shupe M. D, Poellot C. M. R, 8.2 Retrieval of cloud phase over the Arctic using MODIS 6.7-12 µm data, in: Proceedings of the 12th Conference on Atmospheric Radiation, AMS, American Meteorological Society, 2006, paper 8.2. URL `https://www-pm.larc.nasa.gov/ceres/pub/conference/Spangenberg.SMO.06e.pdf`

[8] Pavolonis M. J, Advances in Extracting Cloud Composition Information from Spaceborne Infrared Radiances—A Robust Alternative to Brightness Temperatures. Part I: Theory, Journal of Applied Meteorology and Climatology 49 (9) (2010) 1992 – 2012. `http://dx.doi.org/10.1175/2010JAMC2433.1`.

[9] Rampal N, Davies R, Detecting the Phase of Marine Boundary Layer Clouds: Some Implications for Cloud Albedo, Journal of Geophysical Research: Atmospheres 127 (24) (2022) e2022JD037496. `http://dx.doi.org/10.1029/2022JD037496`.

[10] Verlinde J, Harrington J. Y, McFarquhar G. M, Yannuzzi V. T, Avramov A, Greenberg S, Johnson N, Zhang G, Poellot M. R, Mather J. H, Turner D. D, Eloranta E. W, Zak B. D, Prenni A. J, Daniel J. S, Kok G. L, Tobin D. C, Holz R, Sassen K, Spangenberg D, Minnis P, Tooman T. P, Ivey M. D, Richardson S. J, Bahrmann C. P, Shupe M, DeMott P. J, Heymsfield A. J, Schofield R, The Mixed-Phase Arctic Cloud Experiment, Bulletin of the American Meteorological Society 88 (2) (2007) 205 – 222. `http://dx.doi.org/10.1175/BAMS-88-2-205`.

[11] Menzel W. P, Frey R. A, Baum B. A, Cloud top properties and cloud phase algorithm theoretical basis document, Tech. rep., NASA Goddard Space Flight Center (2015).
URL `https://atmosphere-imager.gsfc.nasa.gov/sites/default/files/ModAtmo/MOD06-ATBD_2015_05_01_2.pdf`

[12] Yang P, Wei H.-L, Baum B. A, Huang H.-L, Heymsfield A. J, Hu Y. X, Gao B.-C, Turner D. D, The spectral signature of mixed-phase clouds composed of non-spherical ice crystals and spherical liquid droplets in the terrestrial window region, Journal of Quantitative Spectroscopy and Radiative Transfer 79-80 (2003) 1171–1188, Electromagnetic and Light Scattering by Non-Spherical Particles. `http://dx.doi.org/10.1016/S0022-4073(02)00348-5`.

[13] Schulz J, Albert P, Behr H.-D, Caprion D, Deneke H, Dewitte S, Dürr B, Fuchs P, Gratzki A, Hechler P, Hollmann R, Johnston S, Karlsson K.-G, Manninen T, Müller R, Reuter M, Riihelä A, Roebeling R, Selbach N, Tetzlaff A, Thomas W, Werscheck M, Wolters E, Zelenka A, Operational climate monitoring from space: the EUMETSAT Satellite Application Facility on Climate Monitoring (CM-SAF), Atmospheric Chemistry and Physics 9 (5) (2009) 1687–1709. `http://dx.doi.org/10.5194/acp-9-1687-2009`.

[14] Minnis P, Hong G, Ayers J. K, Smith W. L, Yost C. R, Heymsfield A. J, Heymsfield G. M, Hlavka D. L, King M. D, Korn E, McGill M. J, Selkirk H. B, Thompson A. M, Tian L, Yang P, Simulations of Infrared Radiances over a Deep Convective Cloud System Observed during TC^4: Potential for Enhancing Nocturnal Ice Cloud Retrievals, Remote Sensing 4 (10) (2012) 3022–3054. `http://dx.doi.org/10.3390/rs4103022`.

[15] Platnick S, Heidinger A, Ackerman S, Amarasinghe N, Dutcher S, Frey R, Hubanks P, Li Y, Marchant B, Meyer K, et al., EOS MODIS and SNPP VIIRS Cloud Properties: User Guide for the Climate Data Record Continuity Level-2 Cloud Top and Optical Properties Product (CLDPROP), Tech. rep., Technical Report, NASA Goddard Space Flight Center, Greenbelt, MD, USA (2019).
URL `https://ladsweb.modaps.eosdis.nasa.gov/api/v2/content/archives/Document%20Archive/Science%20Data%20Product%`

20Documentation/SNPP_CloudOpticalPropertyContinuityProduct_UserGuide_v1.pdf

[16] Negri R, Machado L, Borde R, Inner convective system cloud-top wind estimation using multichannel infrared satellite images, International Journal of Remote Sensing 35 (2) (2014) 651–670. http://dx.doi.org/10.1080/01431161.2013.871391.

[17] Mayer J, Bugliaro L, Mayer B, Piontek D, Voigt C, Bayesian cloud-top phase determination for Meteosat Second Generation, Atmospheric Measurement Techniques 17 (13) (2024) 4015–4039. http://dx.doi.org/10.5194/amt-17-4015-2024.

[18] Knap W. H, Hess M, Stammes P, Koelemeijer R. B, Watts P. D, Cirrus optical thickness and crystal size retrieval from ATSR-2 data using phase functions of imperfect hexagonal ice crystals, Journal of Geophysical Research: Atmospheres 104 (D24) (1999) 31721–31730. http://dx.doi.org/10.1029/1999JD900267.

[19] Virtanen T. H, Kolmonen P, Rodríguez E, Sogacheva L, Sundström A.-M, de Leeuw G, Ash plume top height estimation using AATSR, Atmospheric Measurement Techniques 7 (8) (2014) 2437–2456. http://dx.doi.org/10.5194/amt-7-2437-2014.

[20] Baran A. J, Brown S. J, Foot J. S, Mitchell D. L, Retrieval of Tropical Cirrus Thermal Optical Depth, Crystal Size, and Shape Using a Dual-View Instrument at 3.7 and 10.8 μm, Journal of the Atmospheric Sciences 56 (1) (1999) 92 – 110. http://dx.doi.org/10.1175/1520-0469(1999)056<0092:ROTCTO>2.0.CO;2.

[21] Baran A. J, Havemann S, Francis P, Watts P. D, A consistent set of single-scattering properties for cirrus cloud: tests using radiance measurements from a dual-viewing multi-wavelength satellite-based instrument, Journal of Quantitative Spectroscopy and Radiative Transfer 79-80 (2003) 549–567, Electromagnetic and Light Scattering by Non-Spherical Particles. http://dx.doi.org/10.1016/S0022-4073(02)00307-2.

[22] Copernicus Sentinel-3, SLSTR level-1b product SL_1_RBT [dataset], https://documentation.dataspace.copernicus.eu/Data/

SentinelMissions/Sentinel3.html#sentinel-3-slstr-level-1, European Space Agency (2016).

[23] Sassen K, Wang Z, Classifying clouds around the globe with the CloudSat radar: 1-year of results, Geophysical Research Letters 35 (4) (2008). http://dx.doi.org/10.1029/2007GL032591.

[24] Rozanov V, Rozanov A, Kokhanovsky A, Burrows J, Radiative transfer through terrestrial atmosphere and ocean: Software package SCIATRAN, Journal of Quantitative Spectroscopy and Radiative Transfer 133 (2014) 13–71. http://dx.doi.org/10.1016/j.jqsrt.2013.07.004.

[25] Mei L, Rozanov V, Rozanov A, Burrows J. P, SCIATRAN software package (V4.6): update and further development of aerosol, clouds, surface reflectance databases and models, Geoscientific Model Development 16 (5) (2023) 1511–1536. http://dx.doi.org/10.5194/gmd-16-1511-2023.

[26] Mishchenko M. I, Dlugach J. M, Yanovitskij E. G, Zakharova N. T, Bidirectional reflectance of flat, optically thick particulate layers: an efficient radiative transfer solution and applications to snow and soil surfaces, Journal of Quantitative Spectroscopy and Radiative Transfer 63 (2) (1999) 409–432. http://dx.doi.org/10.1016/S0022-4073(99)00028-X.

[27] Yang P, Bi L, Baum B. A, Liou K.-N, Kattawar G. W, Mishchenko M. I, Cole B, Spectrally Consistent Scattering, Absorption, and Polarization Properties of Atmospheric Ice Crystals at Wavelengths from 0.2 to 100 µm, Journal of the Atmospheric Sciences 70 (1) (2013) 330 – 347. http://dx.doi.org/10.1175/JAS-D-12-039.1.

[28] Segelstein D. J, The complex refractive index of water, Master's thesis, University of Missouri, Kansas City (1981).
URL https://mospace.umsystem.edu/xmlui/handle/10355/11599

[29] Warren S. G, Brandt R. E, Optical constants of ice from the ultraviolet to the microwave: A revised compilation, Journal of Geophysical Research: Atmospheres 113 (D14) (2008). http://dx.doi.org/10.1029/2007JD009744.

[30] Inoue T, A cloud type classification with NOAA 7 split-window measurements, Journal of Geophysical Research: Atmospheres 92 (D4) (1987) 3991–4000. `http://dx.doi.org/10.1029/JD092iD04p03991`.

[31] de Castro, Antonio J., Briz, Susana, Fernández-Gómez, Isabel, Rodríguez, Irene, López, Fernando, for JEM-EUSO Collaboration, Cloud phase identification based on brightness temperatures provided by the bi-spectral IR Camera of JEM-EUSO Mission, EPJ Web of Conferences 89 (2015) 03002. `http://dx.doi.org/10.1051/epjconf/20158903002`.

Cloud phase classification using SLSTR measured brightness temperatures at 3.74, 10.85, 12.00 μm

Kameswara S. Vinjamuri[a], Marco Vountas[a], Vladimir Rozanov[c,1], Luca Lelli[b], Hartmut Boesch[a], John P. Burrows[a]

[a]Institute of Environmental Physics, University of Bremen, Bremen, Germany
[b]Remote Sensing Technology Institute, German Aerospace Centre (DLR), Wessling, Germany
[c]Independent Researcher, Bremen, Germany
[1]Formerly with the Institute of Environmental Physics (IUP), University of Bremen, Bremen, Germany

Acknowledgments

We gratefully acknowledge the funding by the Deutsche Forschungsgemeinschaft (DFG, German Research Foundation) - Projektnummer 268020496 - TRR 172, within the Transregional Collaborative Research Center "ArctiC Amplification: Climate Relevant Atmospheric and SurfaCe Processes, and Feedback Mechanisms (AC)3".

We gratefully acknowledge the

- The European Space Agency (ESA) for the Sentinel-3 mission, with special thanks to the SLSTR team.

- NASA for the CloudSat and CALIPSO missions. Acknowledgments to the CloudSat Data Processing Center for providing the 2B-CLDCLASS-LIDAR data.

- The State and the University of Bremen for their support and funding of this research.

This study was made possible by the use of a high-performance computing (HPC) system. We would like to thank the DFG for providing the HPC system Hypatia, which was funded under the grant GZ INST 144/493-1 FUGG.

Corresponding author: Kameswara Sarma Vinjamuri,
Institute of Environmental Physics (IUP), University of Bremen
Otto-Hahn-Allee 1, 28359 Bremen, Germany
Email: kamesh@iup.physik.uni-bremen.de

Highlights

- Directional brightness temperature difference at 3.74 μm can be used to separate water and ice clouds. When used with brightness temperature differences at 10.85 μm and 12.00 μm, mixed-phase clouds can be identified.

- Mixed-phase clouds occurring at lower cloud top heights are challenging to separate from water clouds.

Author Statement

Manuscript Number: JQSRT-D-25-00365

TITLE: Cloud phase classification using SLSTR measured brightness temperatures at 3.74, 10.85, 12.00 µm

Kameswara Sarma Vinjamuri: Conceptualization, Methodology, Software, Formal analysis, Visualization, Writing - Original Draft
Marco Vountas: Conceptualization, Supervision, Writing-Review & Editing
Vladimir Rozanov: Software, Writing-Review & Editing
Luca Lelli: Writing-Review & Editing
Hartmut Boesch: Supervision, Writing-Review & Editing
John P. Burrows: Conceptualization, Supervision, Writing-Review & Editing

Declaration of interests

☒ The authors declare that they have no known competing financial interests or personal relationships that could have appeared to influence the work reported in this paper.

☐ The authors declare the following financial interests/personal relationships which may be considered as potential competing interests: